Visualising Macroscopic Inhomogeneities in Perovskite Solar Cells

Akash Dasgupta[1†] and Suhas Mahesh[1,2†],Pietro Caprioglio[1], Yen-Hung Lin[1], Karl-Augustin Zaininger[1], Robert D.J. Oliver[1], Philippe Holzhey[1], Suer Zhou[1], Melissa M. McCarthy[1], Joel A. Smith[1], Maximilian Frenzel[1,3], M. Greyson Christoforo[1], James M. Ball[1], Bernard Wenger[1] and Henry J. Snaith[1]

† Both these authors contributed equally.

1. Department of Physics, University of Oxford, Clarendon Laboratory, Parks Road, Oxford, OX1 3PU, UK

2. Edward S. Rogers Sr. Department of Electrical & Computer Engineering, University of Toronto, 10 King's College Rd, Toronto, ON M5S 3G8, Canada

3. Department of Physical Chemistry, Fritz Haber Institute, Faradayweg 4-6, 14195 Berlin, Germany

Abstract

Despite the incredible progress made, the highest efficiency perovskite solar cells are still restricted to small areas (<1 cm^2). In large part, this stems from a poor understanding of the widespread spatial heterogeneity in devices. Conventional techniques to assess heterogeneities can be time consuming, operate only at microscopic length scales, and demand specialist equipment. We overcome these limitations by using luminescence imaging to reveal large, millimetre scale heterogeneities in inferred electronic properties. We determine spatially resolved maps of '*charge collection quality*', measured using the ratio of photoluminescence intensity at open and short-circuit. We apply these methods to quantify the inhomogeneities introduced by a wide range of transport layers, thereby ranking them by suitability for upscaling. We reveal that top-contacting transport layers are the dominant source of heterogeneity in the multi-layer materials stack. We suggest that

this methodology can be used to accelerate the development of highly-efficient, large area modules, especially through high-throughput experimentation.

TOC Graphic

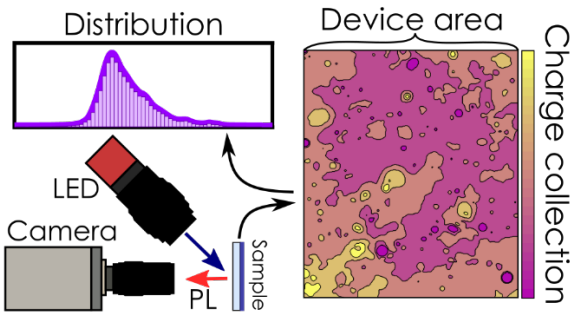

Photovoltaic (PV) deployment at the multi-terawatt scale is of crucial importance in the quest to transition to a zero-carbon economy[1]. Since power conversion efficiency (PCE) is one of the biggest determinants for the price of electricity per kWh, and therefore real-world adoption, developing highly efficient module-scale photovoltaics is a crucial avenue of research. While it took 60 years to engineer c-Si PV with a PCE of 26.7%[2], it took hybrid perovskite PV only a decade to surpass 25.5%[2]. Apart from the inherent high-quality optoelectronic properties of hybrid perovskites, a key factor behind this rapid efficiency increase has been the broad suite of characterisation methodologies developed by the semiconductor community which reduces reliance upon trial-and-error experimentation. As instrumentation and our understanding of semiconductor processes advance, new characterisation methods may emerge, offering powerful new ways to accelerate materials discovery and optimisation.

A fundamental principle, which has only become commonly exploited over the last ten years, is that a good solar cell is also a good light emitting diode[3,4]. This is because the trap states which capture excited charge carriers and reduce the amount of extractable work in a solar cell, also facilitate recombination that does not emit photons. Thus, photoluminescence

quantum efficiency ($PLQE$) serves as an excellent proxy for the quality of photovoltaic materials or devices. Indeed, luminescence measurements have emerged as a powerful "contactless probe" of loss mechanisms [5]. Since spontaneous emission is linked to physical quantities such as the carrier densities, the density of states, traps, and the quasi-fermi level splitting ($QFLS$), many internal properties and processes can be deduced from the luminescence [6]. This approach will only become more powerful as luminescence efficiencies improve and cells approach their thermodynamic limiting efficiencies.

While incredible advances have been made in PCEs, highly efficient perovskite solar cells are still restricted to small active areas (≤1 cm^2). The simple nature of the processing techniques used for some emerging technologies such as metal halide perovskites introduces large local fluctuations both at short (<100 nm) and long length scales (>10 µm)[7,8]. Even well-performing perovskite solar cells are seen to exhibit regions both of high and poor luminescence efficiencies. Understanding the origins of and overcoming these heterogeneities is key to translating high-efficiency lab technology to wafer and full module scale manufacturing (~250 to 20,000 cm^2).

A significant barrier to such upscaling is the lack of advanced characterisation methods that can perform high-throughput measurements on an appropriate length scale. Maps of spatially resolved voltage loss have been constructed using hyperspectral luminescence imaging [9] and light-beam induced current (LBIC) has been used in Si [10] and perovskites[11] to spatially map short-circuit current. These techniques, however, can be time consuming (order of hours) and require access to specialist equipment.

Spatially resolved luminescence measurements provide a fast (~mins) and relatively simple method for characterising performance parameters and have been used in Si cells for a long time to identify series resistance hotspots in wafers [12–15]. In emerging PV materials like

perovskites, imaging of the PL over very small (nm to micrometre) length scales has produced maps of parameters such as $QFLS$[8,16]. Heterogeneities in luminescence on a device scale (> 1 mm) have also been measured, but many images of luminescence are presented in entirely arbitrary units, and comparison with established mapping techniques or integrated measurements are necessary for more robust analysis beyond simply identifying regions of low luminescence[16–19]. Indeed, a review of mapping techniques in perovskites [20] found that while luminescence measurements have been used effectively to map voltage losses on microscopic length scales, such maps are not well-established at macroscopic length-scales.

Spatially resolved maps of parameters such as the ideality factor have been produced[21], which can be used to understand the recombination mechanisms in a device. In terms of current loss, the optically measured parameter "current transport efficiency" (f_T) introduced by Wong and Green[22,23] as a figure of merit. f_T was conceptualised for Si p-n junction cells, defined as the differential ratio of the extracted (δJ) current to the light induced current (δJ_L), over an infinitesimally small voltage step, capturing losses in transporting the current from the p-n junction to the load at some voltage bias. Spatially resolved maps of f_T have been applied in Si[24] and later in perovskites . El-Hajje et.al measured spatially resolved maps of f_T in perovskite solar cells, across both a micron and mm length scale, evaluated near open-circuit[25]. Ren et.al measured similar maps near maximum power point, for a range of intensities, and suggest the differences in f_T observed in the samples of the study results from a difference in series resistance[26].These maps of f_T provide a good way to probe the effects of factors such as series resistance at different voltage points. However, at short-circuit, current loss is unlikely to be dominated by the effect of series resistance (see Supplementary note 1) . Additionally, δJ_L as defined in the formulisation of f_T refers to the

current which flows through the p-n junction. In the case of perovskite solar cells, this is likely to correspond to current which is extracted at the transport layer, and therefore losses in current due to charge carriers not reaching these layers, and remaining in the bulk, is not captured by this factor. The anomalous PL observed in many perovskite solar cells[27–29] , which has been linked to loss in short-circuit current, is likely to have contributions from carriers never reaching the charge extraction layers.

In this work, we introduce a relatively simple methodology by which we use a sensitive optical camera to image the luminescence of operational perovskite solar cells under varying optical irradiance and electrical bias. By applying the principle of detailed balance, we are able to derive spatial maps of many important optoelectronic and device parameters. We experimentally demonstrate that the ratio of short-circuit $PLQE$ to open-circuit $PLQE$ is an excellent measure of the effectiveness with which generated charge is collected in the case of perovskite solar cells, and use this parameter to generate spatially resolved maps of current loss across cm scale images. Furthermore, we show how spatially resolved maps of parameters, such as $QFLS$ and ideality factor, can be effectively used to reveal correlations between parameters by using a large amount of data extracted from measurements on a single sample. We also visualise the inhomogeneities introduced when seven widely employed charge transport layers (tin oxide nanoparticles (**SnO_2 NP**), C_{60}, 2,2',7,7'-tetrakis[N,N-di(4-methoxyphenyl)amino]-9,9'-spirobifluorene (**spiro-OMeTAD**), nickel oxide (**NiO_x**), poly[bis(4-phenyl)(2,4,6-trimethylphenyl)amine], (**PTAA**), poly(N,N'-bis-4-butylphenyl-N,N'-bisphenyl)benzidine (**poly-TPD), C_{60}** and Phenyl-C61-butyric acid methyl ester (**PCBM**)) are processed into a partial device stack and we use quantitative metrics to describe this inhomogeneity. This can serve as a useful metric to rank materials and

processing routes by suitability for upscaling. This is an important complement to the macroscopic quantification of the non-radiative recombination introduced by each layer— a technique already widely used by the community.

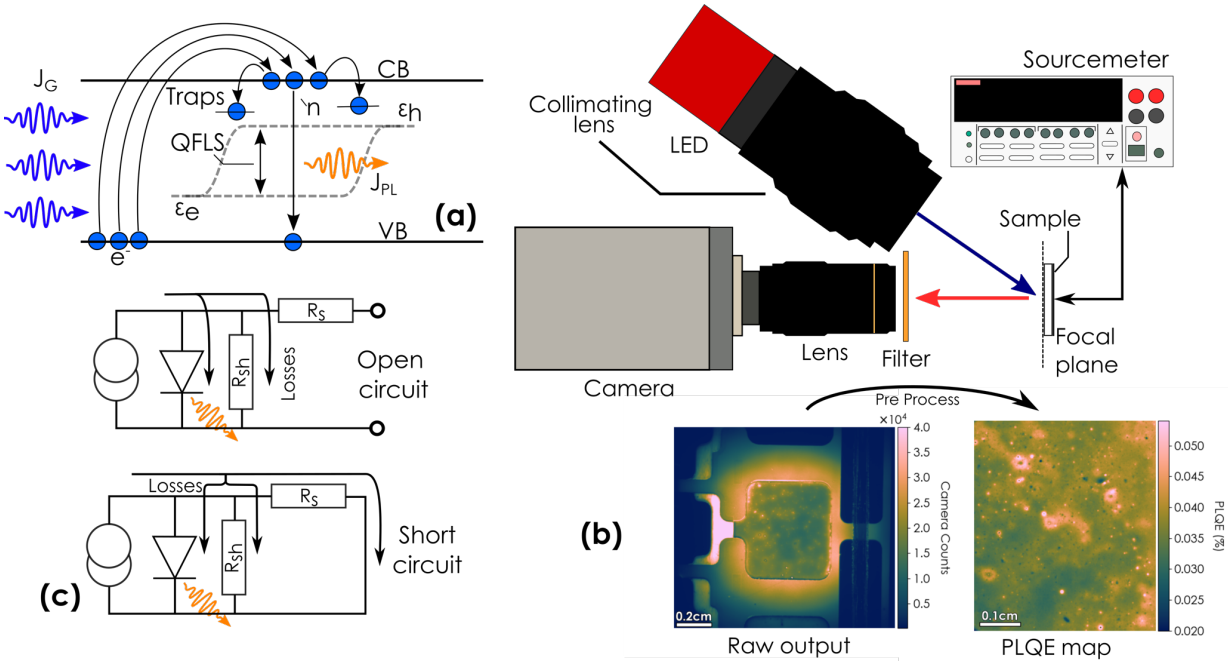

Figure 1 (a) Schematic of QFLS induced by optically excited carriers. Sub bandgap states can mediate fast non-radiative recombination which drains the bands of excited carriers. This changes the carrier concentration, which is also linked to the PLQE, making the PLQE an effective probe of both QFLS and charge carrier dynamics. (b) Schematic of luminescence imaging setup. Images are taken using an image sensor and lens, with a long pass filter to block the 440nm excitation light. The sample can be electrically biased using a source meter. A white diffuse reflector reference is used to calibrate the camera in order to determine the absolute luminescence and hence make maps of the PLQE. (c) Equivalent circuit diagram for a simple solar cell at open and short-circuit. PL occurs when current flows through the diode. PL at open-circuit is reduced due to the shunt path, PL at short-circuit may be affected by both.

We combine luminescence measurements with detailed balance calculations to create maps of the following parameters which link directly to PV performance losses: $\boldsymbol{QFLS}$ **at open-circuit**, which is closely linked to V_{OC} loss; **charge collection quality**, a metric linked to J_{SC} loss; and the **ideality factor** n, which encodes information about the dominant recombination mechanism in the material. The $QFLS$ and ideality factor maps are produced in this work using adaptations of methods previously reported [30–33]. The luminescence-

derived charge collection quality is a new metric that we introduce and will be justified and experimentally validated in a later section.

When charge carriers are optically excited in a solar cell, the chemical potentials of electrons and holes become non-identical ('quasi-fermi levels'). The difference between these two quasi-fermi levels ('quasi-fermi level splitting') is equal to $e \cdot V_{OC}$ in an ideal device, where e is the elementary charge (Figure 1a). However, misalignment of energy levels at the interfaces or lack of selectivity of the charge extraction heterojunctions often causes $e \cdot V_{OC}$ to be lower than the internal $QFLS$[30,34].

The principle of optoelectronic reciprocity [4,32,35] allows us to link the internal $QFLS$ to the photoluminescence quantum efficiency ($PLQE$):

$$QFLS = QFLS_{rad} + kT \ln(PLQE), \quad (1)$$

where $QFLS_{rad}$ is the $QFLS$ in the radiative limit, which can be calculated from the active material's absorption spectrum [32,36], and k is the Boltzmann constant. A more thorough derivation of Equation 1 is given in Supplementary note 2. A schematic of this process is shown in Figure 1a. A spatially resolved map of the $PLQE$ therefore allows us to reconstruct a map of the $QFLS$. This is a contactless measurement, and so can be done for "half-stacks" (partially constructed solar cells) as well as full devices.

The nature of dominant charge recombination mechanism in the device can be inferred from the ideality factor (n). The ideality factor features in the classical diode equation:

$$J_D = J_0 \left(e^{\frac{eV_D}{nkT}} - 1 \right), \quad (2)$$

where J_D, V_D are the diode current and voltage respectively, J_0 is the diode saturation current, and T is the temperature of the cell. The ideality factor, which is unity in an ideal cell, was traditionally understood to tend towards 2 with increasing first order non-radiative

recombination, understood through the Shockley-Read-Hall model[37,38]. However recent reports[31,39] have provided greater clarity by distinguishing between the influence of bulk and interfacial recombination (occurring at the perovskite/transport layer interface) on the ideality factor.

The ideality factor may be found optically using a method applied by Sarritzu[32], with the relation:

$$\ln(I_{suns}) + C = \frac{QFLS}{nkT}, \tag{3}$$

Here, I_{suns} is the illumination irradiance expressed as number of suns (1 sun is AM1.5 100 mWcm^{-2} equivalent irradiance for that bandgap), and C a constant term. A more thorough derivation of Equation 3 is also given in Supplementary note 2. Thus, the ideality factor for each point on the active area can be calculated using intensity dependant $QFLS$ maps. The distribution of n vs $QFLS$ therefore gives us information about the dominant type of recombination.

For our imaging setup (Fig 1b) we used a sensitive Si CMOS camera (Andor Zyla 4.2, Oxford Instruments)[40], which is suitable for low intensity acquisitions. Samples can be imaged under both controlled optical excitation (440nm LED; 0-1 sun equivalent photon flux) and electrical bias. In the case of full devices, we used the test device itself to calibrate the optical intensity in terms of number of suns by comparing the short-circuit current to the short-circuit current measured on a well calibrated solar simulator. A long pass filter is used in the imaging set up to block the 440nm excitation light from reaching the camera.

The number of counts recorded by each camera pixel scales linearly with the number of photons emitted by the associated point on the sample, assuming that the signal is significantly larger than the noise floor. The sample is aligned to be in the focal plane of the

lens and coincides with the centre of the illumination, where the illumination profile has the flattest intensity profile (see Figure S3).

When the $PLQE$ is desired, a high reflectance $BaSO_4$ plate is imaged without filtering as a reference. A more detailed description, including correction factors used can be found in Supplementary note 3.

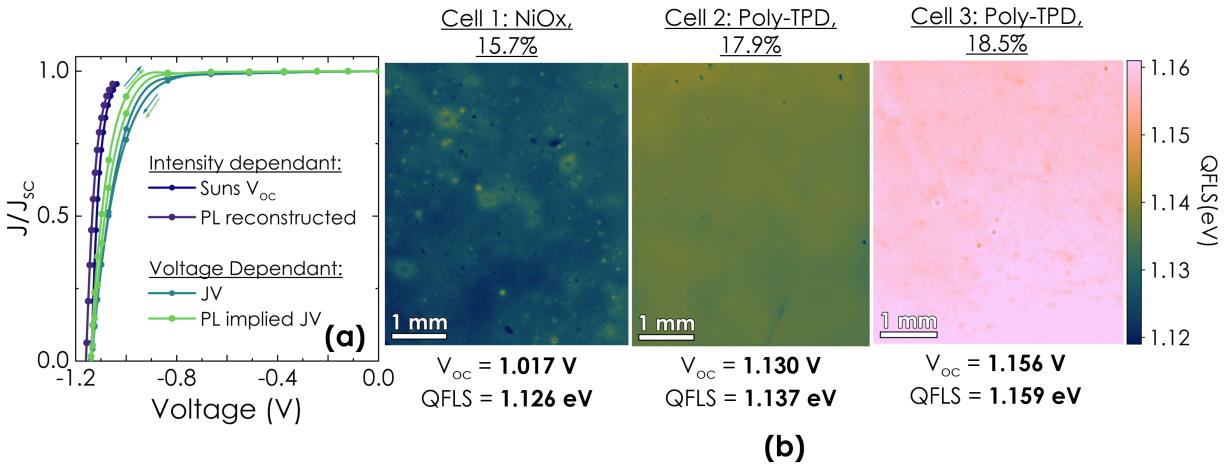

Figure 2: Reconstructed JV curves and QFLS maps measured under 1 sun illumination. ***(a)*** *The current-voltage response of a 1.6 eV bandgap $FA_{0.83}Cs_{0.17}Pb(I_{0.83}Br_{0.17})_3$ perovskite solar cell measured in four different ways. The Suns-V_{OC} curve was constructed by measuring the V_{OC} across a range of illumination intensities. The 'PL reconstructed' curve (optical version of Suns-V_{OC}) was constructed from the QFLS at open-circuit measured at different illumination intensities. The 'PL implied JV' was constructed using the method described by Stolterfoht et al.[27] which links PL intensity at different voltages to the extracted current. The arrows indicate the direction of the scan.* ***(b)*** *QFLS maps from 1.6 eV bandgap FACs mixed halide perovskite solar cells, with NiO_x (Cell 1) and poly-TPD (cells 2,3) as HTLs. All use a PCBM/BCP/Au top contact.*

Before undertaking this work, we were not certain what features and inhomogeneities would exist at the 0.01–1 mm length scale that our imaging setup resolves. In order to verify the general validity of our approach, we recorded luminescence images on a selection of different perovskite solar cells. We imaged a well performing $FA_{0.83}Cs_{0.17}Pb(I_{0.83}Br_{0.17})_3$ device (18.5% PCE, 1.6 eV bandgap, see Fig S5 and table S3 in SI) and characterised the current-voltage response in four different ways (Fig 2a): two electrical measurements under illumination, and two optical measurements analogous to the electrical measurements. The

two electrical measurements include: 1. Measuring the current while sweeping the voltage (labelled '**JV**') 2. Measuring the V_{OC} while sweeping intensity, which is used to infer the current density (also known as the **Suns-V_{OC}** method [41]). The corresponding optical measurements include: 1. Inferring the current density from the PL intensity averaged across the device as the voltage was swept (drawing upon the approach of Stolterfoht et al.[27], labelled '**PL implied JV**') 2. Inferring voltage from the average $PLQE$ at open-circuit while the illumination intensity is changed (using Equation 1 and taking the $QFLS$ to be the voltage; labelled '**PL reconstructed**').

The curves measured by all four methods vary as would be expected from macroscopic measurements of the same properties. Furthermore, the electrically measured curves show excellent agreement with the curves derived from averaging the PL images (Figure 2a). The fill-factor appears enhanced in the Suns-V_{OC} and PL-reconstructed curves as these measurements were performed at open-circuit where series resistance has no influence. This validates our setup's ability to measure absolute PL intensities and reconstruct the $QFLS$ across a range of bias conditions.

To further validate the setup and assess the types of inhomogeneities present in full devices, we reconstructed $QFLS$ maps at 1 sun illumination for 1.6 eV bandgap cells of two different architectures (Figure 2b): **cell 1**: NiO_x/perovskite/[6,6]-phenyl-C_{61}-butyric acid methyl ester (PCBM), **cells 2,3**: poly-TPD/perovskite/PCBM.

In all the captured PL images, we observe a number of spatial inhomogeneities at the mm length scale, with the better-performing poly-TPD cells exhibiting a more homogenous $QFLS$ distribution compared to the NiO_x cell. In a later section, we present a fuller analysis of the heterogeneity introduced by all the widely used transport layers. When comparing the two poly-TPD cells, we can see that despite identical processing conditions, the

variability is still quite different. This is a common feature of devices processed by simple methods like solution processing and is likely to be a significant barrier to scale-up.

The poorly performing NiO_x-based cell also has a larger difference between the mean $QFLS$ and measured, indicating energy level misalignment at a heterojunction or lack of charge selectivity[30,34]. Notwithstanding this small difference, the average values of the $QFLS$ are still close to the measured V_{OC}, and they agree very well for both the poly-TPD-based cells, once again validating our ability to correctly reproduce $QFLS$ maps.

Furthermore, though the luminescence is rather inhomogeneous in the NiO_x based cell, there are localised regions on the map that approach the luminescence efficiencies of the well-performing poly-TPD-based cells. Their existence indicates that an intrinsic limitation of the material is not at work here: with optimization of processing conditions, we can expect to fabricate a device with uniformly bright luminescence. We suggest that such luminescence imaging could be combined with deposition equipment so that performance can continuously be monitored in-situ, accelerating device optimisation. With the rise of laboratory automation, we can also envision that such luminescence images will be fed to active learning models that can vary processing parameters until the luminescence is maximised.

While the protocol for making spatial maps of quasi-Fermi level splitting (and hence voltage losses) from luminescence measurements is well-established, a method for estimating total current loss at short-circuit in a spatially resolved fashion has not been successfully applied to perovskites. Here we utilise and experimentally verify an expression that links current loss to luminescence at short circuit, enabling us to visualise regions of current loss over a cell's active area.

An ideal solar cell at short-circuit (SC) collects all the generated carriers and therefore will not emit any photons. In practice, however, perovskite solar cells have been observed to emit significant PL even at short-circuit [27]. Furthermore, a transient increase in PL at short-circuit has been observed for some cell types, in conjunction with a transient increase in current loss[28], and it has been suggested that the ratio of PL at SC to OC may be linked to charge extraction efficiency [29]Similar observations in silicon PV cells have been attributed to diffusion limited carriers generated in the bulk that were unable to reach the p-n junction[9,10], and in some instances the ratio of PL at OC and SC has been used to estimate diffusion lengths in silicon samples.[42] In perovskite devices, one possible explanation for the residual PL at SC could be the screening of the internal field due to ion redistribution, leaving the absorber with a zero net field, where charge can undergo internal recombination before being transported out of the device [28]. Alternatively, perovskite films, due to processing inhomogeneities, may contain regions of isolated material not properly contacted with the electrodes. Rau links this same anomalous 'residual luminescence' observed at short-circuit in Cu(In,Ga)Se_2 solar cells, directly to the ratio of short-circuit current to current generated in the material[43]. In the case of perovskite solar cells, we verify that a similar expression does in fact corelate with losses in short-circuit current, and use it to generate spatially resolved maps of 'current collection' at short-circuit.

We can understand the estimation of current loss intuitively from a comparison between the luminescence intensity from the PV cell at short-circuit and open-circuit. At open-circuit, every generated e-h pair has three possible fates: recombine radiatively, recombine non-radiatively, or flow through the shunt resistance from the equivalent circuit model (Figure 1c). Luminescence can originate only from charge carriers that flow through the diode in the equivalent circuit model.

The extracted current from the cell(J) is linked to the luminescence through the ideality factor, a 'fudge-factor' introduced into the diode equation to account for the mixture of recombination mechanisms that operate in a cell. Comparing the radiative recombination current density (J_{rad}) to total current density J, the PL intensity at open circuit can be shown to be proportional to the generation current (J_G) to the power of n, where n is the ideality factor:

$$J = J_G - J_0 e^{\frac{QFLS}{nkT}}, \qquad J_{rad} = J_0 \cdot EQE_{EL}(V) \cdot e^{\frac{QFLS}{kT}} \tag{4}$$

$$At\ OC: J = 0 \implies J_G = J_0 e^{\frac{QFLS_{oc}}{nkT}} \tag{5}$$

$$\implies J_{rad,oc} = J_0^{1-n} \cdot EQE_{EL}(V) \cdot (J_G)^n \tag{6}$$

since at open-circuit, all generated carriers must recombine.

At short-circuit, the majority of photogenerated charge-carriers are extracted as load current, quenching the PL. Some carriers are not extracted as load current, and instead flow through a shunt pathway or recombine in the perovskite bulk. The current which is not extracted at short-circuit, $J_G - J_{SC}$ is responsible for the anomalous PL at SC:

$$At\ SC: J = J_{sc} \implies J_G - J_{sc} = J_0 e^{\frac{QFLS_{sc}}{nkT}} \tag{7}$$

$$\implies J_{rad,sc} = J_0^{1-n} \cdot EQE_{EL}(V) \cdot (J_G - Jsc)^n \tag{8}$$

Rearranging Equations 6 and 8, we get:

$$J_G - J_{sc} = \left(J_0^{1-n} \cdot EQE_{EL}(V) \cdot J_{rad,sc}\right)^{1/n}, \tag{9}$$

$$J_G = \left(J_0^{1-n} \cdot EQE_{EL}(V) \cdot J_{rad,oc}\right)^{1/n}. \quad (10)$$

Assuming that the ideality factor and $EQE_{EL}(V)$ does not change between OC and SC, we can write:

$$Q_{col} = \frac{Jsc}{J_G} = 1 - \left(\frac{J_{rad,SC}}{J_{rad,OC}}\right)^{\frac{1}{n}} = 1 - \left(\frac{PLQE(SC)}{PLQE(OC)}\right)^{\frac{1}{n}}, \quad (11)$$

where Q_{Col} is a parameter we dub the 'charge collection quality'. In a device with zero series and infinite shunt resistance, Q_{Col} would be identical to the internal quantum efficiency. While Q_{Col} is a function of ideality factor, it remains much faster to measure $PLQE(SC)$ and $PLQE(OC)$ compared to the ideality factor, which requires a full intensity dependant measurement and fitting of the slope of the QFLS as a function of intensity for every pixel in the map. If a fast measurement is required, one can measure only the $PLQE(SC)$ and $PLQE(OC)$, and assume an ideality factor of unity, or any other value that corresponds to the macroscopically averaged ideality factor of the cell, to get an approximate value of Q_{Col}, which still correlates with the current loss (See Supplementary note 5 for full justification). When the effects of shunt and series resistances are included, Q_{Col} can underestimate or overestimate the internal quantum efficiency. Nevertheless, as we shall experimentally demonstrate, it remains a useful metric as it is found to correlate with current loss.

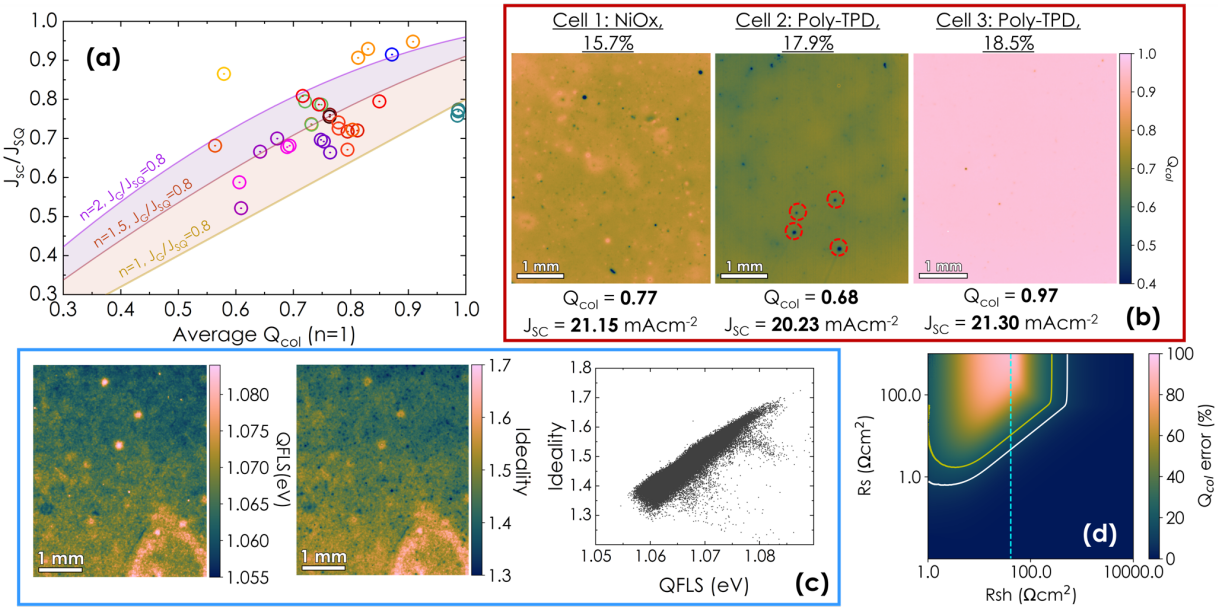

Figure 3 (a) Normalised J_{SC} of different perovskite solar cells vs internal collection quality (averaged across cell area, assuming unity ideality factor). J_{SC} has been normalised to the Shockley–Queisser current, to account for the different bandgaps of cells. Lines drawn indicate the predicted normalised J_{SC} from the measured $Q_{col}|_{n=1}$ from Equation 11, for n=1,1.5 and 2 (assuming the generation current is 80% of the SQ limit max current). Cells from the same substrate are given the same colour (details in SI). All measurements were taken at 1 sun equivilent photon flux, and cells were illuminated for 30s before measurement to bring the device to a steady state (b) Collection quality map of the cells shown in Figure 2. Areas of particularly poor collection quality are highlighted with red circles. Ideality factor maps were incorporated in these measurements. (c) [left to right] Map of QFLS, map of ideality factor and scatter plot of ideality factor vs QFLS, where each data point Is taken from a spatial point from the two maps on the left. (d) The error in the Q_{col} (Qcol – J_{sc}/J_G) as a percentage of Qcol from simulation. White and yellow lines show boundary of 10 and 15 % error. Blue line is the point where for lower shunt resistances, the ratio of current through the shunt Vs through the diode exceeded 1000; For Rsh under the blue line, the PL is under the sensor detector limit.

To experimentally verify the validity of the expression for Q_{Col} (Equation 11), we measured $Q_{Col}\,|_{n=1}$ for a large number of cells, both in positive-intrinsic-negative (p-i-n) and n-i-p architecture, with bandgaps varying from 1.6 to 1.8 eV, with a variety of different hole-transport layers (HTLs) and electron transport layers (ETLs) (see SI for details). For these measurements the ideality factor was considered to be unity, as described. By measuring the average PL intensity over the active area at open-circuit and short-circuit, we can calculate an average $Q_{Col}\,|_{n=1}$ for the device (Equation 11). The relationship between J_{SC}/J_G and $Q_{Col}\,|_{n=1}$ can be calculated, for different 'true' values of ideality factor and accounting

for a reasonable loss in current due to reflection losses and parasitic absorption. If the electrically measured J_{SC} is shown to follow this relation with $Q_{Col}|_{n=1}$, the validity of the expression (Equation 11) is confirmed. To minimise the impact of shunt and series resistance on Q_{Col}, only 'good' devices were chosen, meaning the average shunt resistance may be considered to be much greater than the solar cell's output resistance $\frac{V_{OC}}{I_{SC}}$.

Measurements were made under an equivalent irradiance of 1 sun for each cell, with a pre-illumination of 30s at open-circuit conditions to ensure the device was at steady-state. In Figure 3a, we show a plot of the bandgap-normalised J_{SC} versus the spatially averaged charge collection quality $Q_{Col}|_{n=1}$. The values of $Q_{Col}|_{n=1}$ vs $\frac{J_{SC}}{J_{SQ}}$ fall within a range of values predicted by Equation 11, for ideality factors ranging from 1 to 2, and assuming an average 20% loss in the generation current from the SQ limit (Typical for cells produced in our labs). This confirms the qualitative validity of our expression for Q_{Col}. Apart from variation in ideality factor, we may attribute some of the spread in data to some additional factors, namely varying series and shunt resistances and limitation of setting the intensity to exactly 1 sun.

We now briefly comment on the impact of series and shunt resistances on Q_{Col}.

Luminescence originates from radiative recombination in the semiconductor bulk, which in the equivalent circuit model is a certain fraction of the current flowing through the diode. If a fraction of the current is able to flow through a different pathway, namely the series or shunt resistor, then the luminescence will be altered. At open-circuit, shunt-pathways divert charge away from the perovskite bulk (equivalently more current flows through the shunt resistor as opposed to the diode), diminishing luminescence. Series resistance has no influence at open-circuit. At short-circuit, the presence of a series resistance results in a

non-zero potential difference across the parallel shunt and diode components, hence causing some current to flow through the diode resulting in luminescence at short-circuit, with increasing series resistance. However, even at short-circuit some current will flow through the shunt pathways cause luminescence to diminish which does not correspond to collected current. Using the equivalent circuit model, we can calculate how the internal quantum efficiency $\frac{J_{SC}}{J_G}$ varies with values of R_S and R_{SH}, and compare this to the estimated Q_{Col} (assuming the absolute PL is proportional to current flowing through the diode). Through this, we can estimate the error in Q_{Col} introduced by R_S, R_{SH}. We show that the values for the internal quantum efficiency and Q_{Col} agree with each other very closely (<10% error), apart from the conditions when the shunt resistance is very low, and the series resistance is very high (Figure 3d, see supplementary note 4 for full details). In this case, we found that Q_{Col} tends to overestimate $\frac{J_{SC}}{J_G}$, but this only occurs in extreme cases.

We now comment on the spatial inhomogeneity in Q_{Col} observed in the three cells we present in Figure3a. Since the presence of traps influence device performance on many fronts, it is important to answer the following question: does poor Q_{Col} imply poor $QFLS$, both being mediated by traps? If so, Q_{Col} maps would be unnecessary since $QFLS$ maps essentially provide the same information. Looking at the $QFLS$ and Q_{Col} maps of cell 2 (Figure 2b, 3b), we can see very clearly that this is not the case—regions of poor Q_{Col} are not always detectable on $QFLS$ maps. The red circles in Figure 3b highlight areas where the values of Q_{Col} (and hence the current) is particularly low. These features are completely unobservable with the $QFLS$ map (Figure 2b). Could these low-luminescence regions

instead be explained by shunts? The absence of these features in the map taken at OC (fig 2b) shows that they are not shunts, for shunting effect are active at both OC and SC.

The maps presented (Fig 2b and Fig 3b) indicate that the average value and the inhomogeneity in $QFLS$ (a proxy for V_{OC}) and Q_{Col} (a proxy for J_{SC}) can vary independently in devices, making characterisation of both essential for a full understanding of spatially resolved losses. To illustrate—while cell 2 **(**poly-TPD-based) has superior $QFLS$ as compared to cell 1 **(**NiO_x-based), it has a lower average Q_{Col} (Figure 3b). Furthermore, the two have similar levels of inhomogeneity in Q_{Col}, despite cell 2 having a far more homogenous $QFLS$ map. To reiterate, $QFLS$ and Q_{Col} can vary independently, and both are required to fully map loss mechanisms.

Metrics like Q_{Col} acquire special significance in the context of in-line metrology and high-throughput experimentation. A significant advantage of this approach for identifying inhomogeneities in current loss is that each device measurement requires only a few minutes, in comparison to several hours for an equivalent laser-beam induced current (LBIC) mapping approach.

Besides maps of $QFLS$ and Q_{Col}, , we can study directly maps of ideality factor, which provides information about the recombination processes at work in a solar cell. Plotting the ideality factor vs $QFLS$ for each pixel in the device reveals that more luminescent pixels have higher ideality factors. This trend is evidence that the performance of the cell under measurement is limited by interfacial recombination, and not bulk recombination. This validates a recent study[31] which suggests that in devices dominated by interfacial

recombination, the ideality factor will, rather counter-intuitively, increase with increasing $QFLS$.

Thus the natural spatial variation in solar cell enables us to demonstrate this trend with a large amount of data acquired from only a single device, and in a timespan of minutes. The ability to capture such large amounts of data opens up the possibility of exploring previously unknown relationships between various semiconductor and device properties. There is exciting scope for the application of novel statistical techniques and machine learning methods to analyse such datasets.

Metrics like the charge collection quality Q_{Col} acquire special significance in the context of in-line metrology and high-throughput experimentation. A significant advantage of this approach for identifying inhomogeneities in current loss is that each device measurement requires only a few minutes, in comparison to several hours for an equivalent laser-beam induced current (LBIC) mapping approach.

A priori, the source of this significant inhomogeneity at the 0.1–1 mm scale is unclear. It could be rooted in certain layers, interfaces or be the result of certain processing methods. Such sources of heterogeneity can be characterised by acquiring luminescence maps at each step of solar cell fabrication and quantifying each step's impact on heterogeneity.

We reconstructed $QFLS$ maps for a wide variety of partially and fully fabricated cells, quantitatively measuring the heterogeneity introduced at each stage of device fabrication.

Our study includes seven widely used transport layers (TL) : PCBM, C_{60}, Spiro-OMeTAD, poly-TPD, NiO_x, SnO_2 and PTAA, coated upon or beneath perovskite thin-films as 'half-stacks'. A glass\transparent conductive oxide (TCO)\TL\perovskite stack was used for 'bottom contacting' transport layers and a glass\perovskite\TL stack was used for top contacting layers. For details about the perovskite compositions and fabrication procedures used, see 'Sample fabrication' in the SI. In order to quantify the additional inhomogeneity introduced by a transport layer in contact with these different perovskite films, a reference sample of neat perovskite was deposited on glass in each case.

Luminescence maps of different samples cannot be directly compared for heterogeneity, as the mean value of the $QFLS$ will be different for different samples. Therefore, a normalised measure of spread is needed. The statistical distribution of luminescence data obtained could have a spread that is a function of the mean (for example, in a Poisson distribution the standard deviation is proportional to the root of the mean). In order to compare between different samples, we define the centre normalised $QFLS$:

$$centre\ norm\ QFLS_{i,j} = \frac{QFLS_{i,j} - < QFLS >}{< QFLS >} \quad (7)$$

where i, j are indices of points on the $QFLS$ map, and $< QFLS >$ is the mean $QFLS$ of the sample. The centre normalised $QFLS$ will be centred on 0, and is normalised by the mean, making distributions between different samples comparable.

Maps of centre normalised $QFLS$ are shown in Figure 4, along with corresponding binned distributions with respect to the neat perovskite reference film. We can observe, in general, that each transport layer introduces visibly significant heterogeneity to the neat perovskite on the mm length scale.

The PCBM sample, and to a lesser extent the C_{60} sample, exhibit a large population of bright emissive spots (high QFLS) across its surface. Consequently, the PCBM histogram has a heavy right tail. We interpret these bright speckles to be regions where the fullerene is either not directly electronically contacting, or not present (i.e. pinholes) on top of the perovskite film. In line with the superior homogeneity of C_{60} that we visualise, it is often used as an interlayer alongside an ETL to improve the contact, both in n-i-p[44] and p-i-n architectures [45] , and there is improved performance in devices with evaporated C60 as opposed to solution processed PCBM[46].

The inhomogeneous region in the Spiro-OMeTAD map stretches over 3 mm in length, suggesting that it may be prone to poor electronic contact over large length scales. Half stacks with the bottom contacting layers look comparatively uniform, with the histograms largely resembling the shape of the reference used in each case. Looking at the images however, we can see samples like the NiO_x appear to have more spatial variation over their surface, despite having similar widths in the binned graphs.

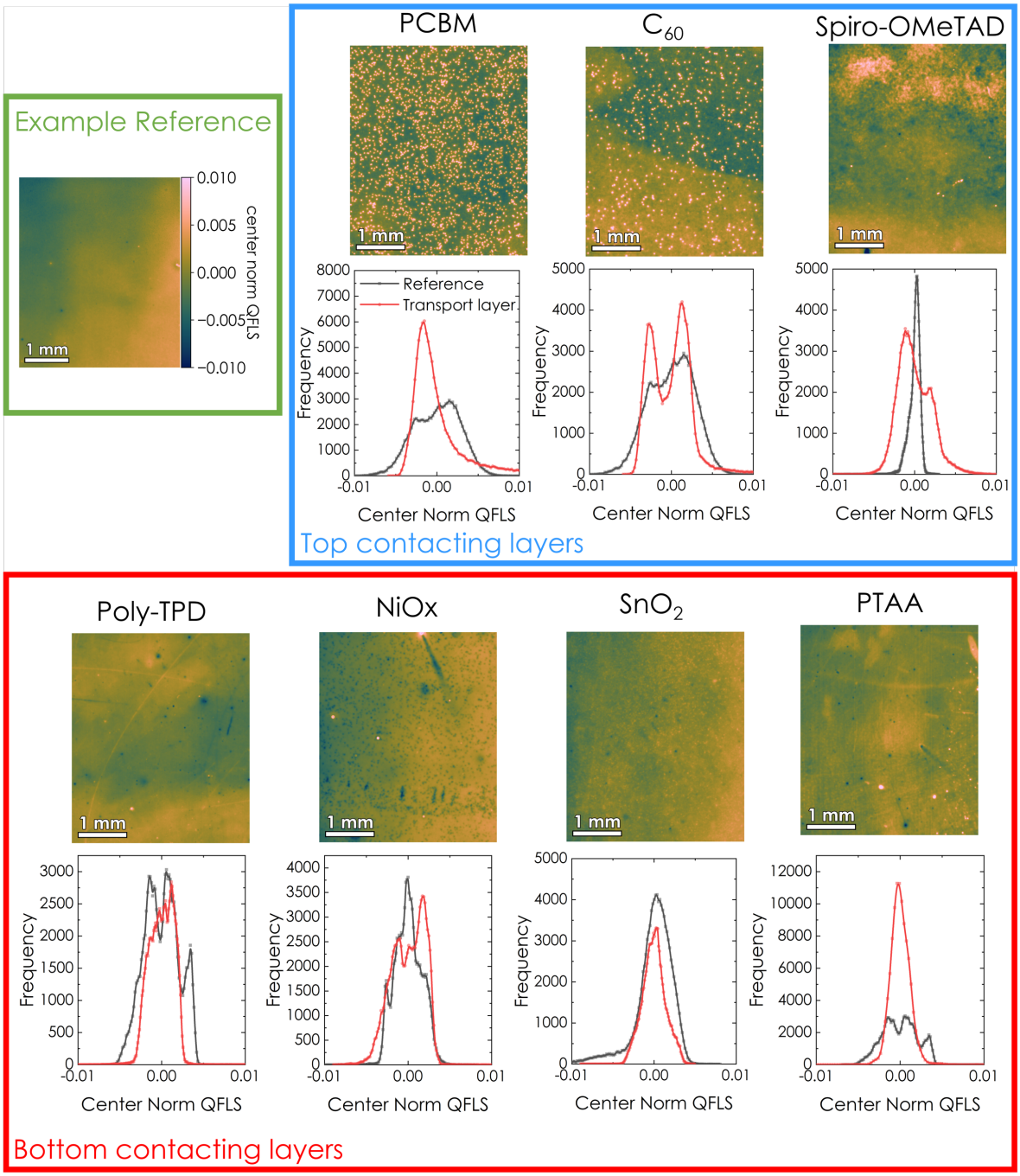

Figure 4: Centre normalised QFLS maps (top, same scale as Example Reference) and histograms of the same maps (bottom) for different transport layer half stacks. Different perovskite blends were used for the samples, so the distribution of a neat perovskite film on glass for each sample is shown on the histograms, and an example reference is shown. The same illumination (1 sun for a 1.6 eV cell) was used for all the samples for consistency, and the colour scale bar is the same for all images (as shown in the example reference).

We can quantify the inhomogeneity in the images by defining:

$$Inhomogeneity\ ratio\ = \frac{\frac{IQR}{< QFLS >}}{\frac{IQR_{ref}}{< QFLS_{ref} >}}, \tag{8}$$

where IQR is the inter quartile range of the $QFLS$ distribution in a map. This metric can be used to quantify the additional inhomogeneity in $QFLS$ introduced when a transport layer is processed, while accounting for the varying mean $QFLS$ found in different samples.

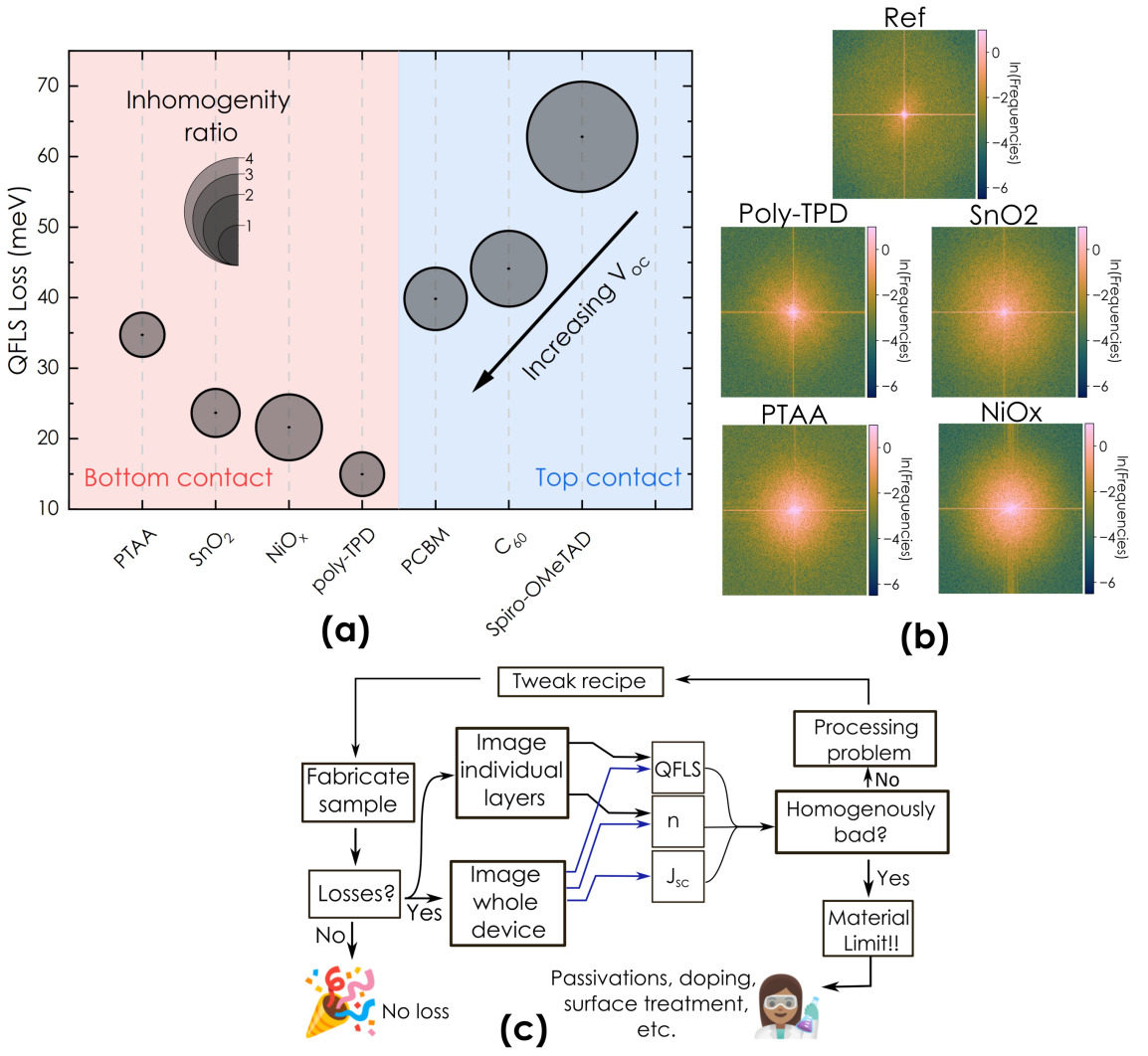

Figure 5 Comparison of the inhomogenity induced by the different transport layers shown in Figure 4. (a) Plot of QFLS loss and inhomogenity ratio for the different transport layers shown in Figure 4. The area of the bubbles is proportional to the inhomogenity of the transport layer (with respect to a reference of the corresponding perovskite on glass). (b) Fourier transforms of the center normalised QFLS maps from Figure 4. The reference shows a strong cross hair pattern typical of a smooth real profile, while all the TLs show some higher frequency terms and the superposition of a gaussian like profile.

Comparing the inhomogeneity introduced by different transport layers, (Figure 5a) we see that bottom contacting layers are fairly benign (inhomogeneity ratio ~ 1), while the top contacting layers, particularly Spiro-OMeTAD, are responsible for significantly more heterogeneity. This contrasting behaviour could be a key determinant that confers upon the n-i-p and p-i-n structures their distinctive advantages and limitations, and merits more detailed investigation.

The presented $QFLS$ histograms encode information about its statistical distribution, but they say nothing about the length-scales over which the variation occurs. In order to quantify the length-scale of variation, we looked at the Fourier transforms (FTs) of the $QFLS$ maps. The FT of a 2D image produces an image of the real image's frequency spectrum, which contains information about the length scale of the changes. Higher intensity further from the centre (high frequency regions) indicates a smaller length scale of change (i.e. sharper changes in QFLS over the sample area). If the length scale of heterogeneity is large (i.e. a relatively unform device), the FT will have high intensities at the centre of the image, and 2 perpendicular lines along the axes forming 'cross hairs' (see Ref in Figure 5b).
The frequency distributions of the TL images all show this same cross hair feature, but have an additional Gaussian-like distribution which extends further into the higher frequencies. The PolyTPD FT closely resembles a uniform device, indicating the QFLS is relatively free of sharply spatial variations. In contrast, the PTAA FT extends further into the higher frequency region revealing sharper spatial variations in QFLS, despite having a similar histogram width to PolyTPD. In summary, the FT of the acquired parameter maps encodes information about the length-scale of variations, and is complementary to the histogram, which encodes the statistical distribution of variations.

While these results cannot be generalised to all possible deposition process for these transport layers, the heterogeneity introduced by a certain transport layer and some deposition specific process be assessed. Based on the capabilities of this technique, we propose an optimisation workflow for identifying and addressing inhomogeneities in a device, illustrated in Figure 5c. If a device shows losses, it may be imaged in the setup, and spatially resolved maps of $QFLS$, collection efficiency, ideality factor, and series resistance (the latter using existing methods [13]) may be produced. If a parameter shows significant inhomogeneity over the device, the fabrication parameters can be iteratively modified using Bayesian optimisation. The process may be repeated, with half stacks being imaged in addition to complete device stacks, to identify which specific problematic layers. If the cells are fully homogenous and losses still persist, alternative materials or chemistries, such as new surface treatments or alternative transport layers, should be attempted.

To summarise, scale-up of perovskite PV to the module scale (~2 m^2) while retaining high efficiencies (>23%) is key to commercialisation and terawatt scale deployment. In order to visualise heterogeneities over entire cell areas, we utilise a fast and relatively simple luminescence imaging method to produce maps of device-relevant parameters.

Our imaging reveals that perovskite cells exhibit significant spatial heterogeneities in V_{OC} and charge collection at the 0.1-1 mm length scale. We experimentally demonstrate that the ratio of PLQE at short-circuit and open-circuit can serve as an excellent indicator of current loss in perovskite solar cells. This enables us to visualise J_{SC} loss over the active area, providing a very useful complement to established V_{OC} mapping methods.

While inhomogeneities in the active layer have been imaged before, the effect of processing steps and transport layers is still uninvestigated. We quantified the heterogeneity introduced when seven widely used transport layers are processed, thereby ranking them by suitability for upscaling. We find that top-contacting transport layers are the dominant source of heterogeneity in the stack. For instance, Spiro-OMeTAD causes a 4-fold increase in heterogeneity when processed. In contrast, bottom-contacting layers are found to be relatively benign. This contrasting behaviour could be a key determinant that confers upon the n-i-p and p-i-n structures their distinctive advantages and limitations, and merits further investigation.

In comparison to slow (~hours) traditional mapping methods like Laser-Beam Induced Current (LBIC), luminescence imaging is fast (~mins) and generates large amounts of data. By using such data gathered on a single device, we were able to validate the relationship between ideality factor and QFLS. We believe that our relatively simple technique will be easy to implement for many scientists and development engineers, to use in combination with process development and high-throughput experimentation, in order to accelerate both lab research and industrial scale-up.

Associated content

Supporting information

Sample fabrication processes; Detailed setup and measurement procedure; Supplementary note on Wong-Green formalism; Supplementary note on theory of luminescent imaging; Illumination profile of setup; Spectral response of setup; Supplementary note on calculating PLQE maps using white reference; JV curves of main cells mapped; JV parameters of main cells mapped; Supplementary note on effect of series and shunt resistance on Q_{col};

Supplementary note on error in Q_{col} maps due to uniform, unity ideality factor assumption; Linearity of camera response; Spectrum of illumination source; Error in PLQE maps due to optical losses not accounted for; Validation of electronics of setup through JV measurement; Example ideality factor calculation from averaged value; PLQE maps at open and short circuit of all cells used in Q_{col} static plot;

Notes

H.J.S. is co-founder and CSO of Oxford PV Ltd.

Acknowledgements

This work was part funded by EPSRC, UK under grant number EP/S00497/1 and the UKRI Global Challenge Research Fund project EP/P032591/1. A.D. and R.D.J.O. would like to express their gratitude to the Penrose scholarship for very generously funding their studentship. S.M. acknowledges the support of the Rhodes Scholarship and the Schmidt Science Fellowship. The research leading to these results has also received funding from the European Union's Horizon 2020 research and innovation programme MAESTRO under the Marie Skłodowska-Curie grant agreement No 764787.

Perceptually uniform colourmap used in this work were kindly developed under the MIT licence by Fabio Crameri [47]. Emoji artwork used in Figure 5 was taken from the 'Google Noto font' suite [48], which is provided as free and open source under the Apache license, version 2.0.

References

(1) Haegel, B. N. M.; Margolis, R.; Buonassisi, T.; Feldman, D.; Garabedian, R.; Green, M.; Glunz, S.; Henning, H.; Holder, B.; Kaizuka, I.; Kroposki, B.; Matsubara, K.; Niki, S.; Sakurai, K.; Schindler, R. A.; Tumas, W.; Weber, E. R.; Wilson, G.; Woodhouse, M.; Kurtz, S.; Haegel, N. M.; Margolis, R.; Buonassisi, T.; Feldman, D.; Froitzheim, A.; Garabedian, R.; Green, M.; Glunz, S.; Henning, H.; Holder, B.; Kaizuka, I.; Kroposki, B.; Matsubara, K.; Niki, S.; Sakurai, K.; Schindler, R. A.; Tumas, W.; Weber, E. R.; Wilson,

G.; Woodhouse, M.; Kurtz, S. Terawatt-Scale Photovoltaics: Trajectories and Challenges. *Science (1979)* **2017**, *356* (6334), 141–143.
(2) Best Research-Cell Efficiency Chart https://www.nrel.gov/pv/cell-efficiency.html (accessed 2021 -10 -27).
(3) Yablonovitch, E.; Miller, O. D.; Miller, O. D.; Miller, O. D. The Opto-Electronics Which Broke the Efficiency Record in Solar Cells. *Conference on Lasers and Electro-Optics 2012 (2012), paper CF2J.1* **2012**, CF2J.1.
(4) Rau, U. Reciprocity Relation between Photovoltaic Quantum Efficiency and Electroluminescent Emission of Solar Cells. *Physical Review B - Condensed Matter and Materials Physics* **2007**, *76* (8), 085303.
(5) Kirchartz, T.; Márquez, J. A.; Stolterfoht, M.; Unold, T. Photoluminescence-Based Characterization of Halide Perovskites for Photovoltaics. *Advanced Energy Materials* **2020**, *10* (26), 1904134.
(6) Peter Würfel, U. W. Physics of Solar Cells: Basic Principles to Advanced Concepts, 3rd Edition. **2016**, 288.
(7) Tennyson, E. M.; Doherty, T. A. S.; Stranks, S. D. Heterogeneity at Multiple Length Scales in Halide Perovskite Semiconductors. *Nature Reviews Materials 2019 4:9* **2019**, *4* (9), 573–587.
(8) Frohna, K.; Anaya, M.; Macpherson, S.; Sung, J.; Doherty, T. A. S.; Chiang, Y.-H.; Winchester, A. J.; Orr, K. W. P.; Parker, J. E.; Quinn, P. D.; Dani, K. M.; Rao, A.; Stranks, S. D. Nanoscale Chemical Heterogeneity Dominates the Optoelectronic Response of Alloyed Perovskite Solar Cells. *Nature Nanotechnology 2021 17:2* **2021**, *17* (2), 190–196.
(9) Stolterfoht, M.; Wolff, C. M.; Márquez, J. A.; Zhang, S.; Hages, C. J.; Rothhardt, D.; Albrecht, S.; Burn, P. L.; Meredith, P.; Unold, T.; Neher, D. Visualization and Suppression of Interfacial Recombination for High-Efficiency Large-Area Pin Perovskite Solar Cells. *Nature Energy* **2018**, *3* (10), 847–854.
(10) Padilla, M.; Michl, B.; Thaidigsmann, B.; Warta, W.; Schubert, M. C. Short-Circuit Current Density Mapping for Solar Cells. *Solar Energy Materials and Solar Cells* **2014**, *12* (PART A), 282–288.
(11) Mundt, L. E.; Kwapil, W.; Yakoob, M. A.; Herterich, J. P.; Kohlstadt, M.; Wurfel, U.; Schubert, M. C.; Glunz, S. W. Quantitative Local Loss Analysis of Blade-Coated Perovskite Solar Cells. *IEEE Journal of Photovoltaics* **2019**, *9* (2), 452–459.
(12) Kampwerth, H.; Trupke, T.; Weber, J. W.; Augarten, Y. Advanced Luminescence Based Effective Series Resistance Imaging of Silicon Solar Cells. *Applied Physics Letters* **2008**, *93* (20), 202102.
(13) Trupke, T.; Pink, E.; Bardos, R. A.; Abbott, M. D. Spatially Resolved Series Resistance of Silicon Solar Cells Obtained from Luminescence Imaging. *Applied Physics Letters* **2007**, *90* (9), 093506.
(14) Würfel, P.; Trupke, T.; Puzzer, T.; Schäffer, E.; Warta, W.; Glunz, S. W. Diffusion Lengths of Silicon Solar Cells from Luminescence Images. *Journal of Applied Physics* **2007**, *101* (12), 123110.
(15) Fuyuki, T.; Kondo, H.; Yamazaki, T.; Takahashi, Y.; Uraoka, Y. Photographic Surveying of Minority Carrier Diffusion Length in Polycrystalline Silicon Solar Cells by Electroluminescence. *Applied Physics Letters* **2005**, *86* (26), 262108.
(16) Draguta, S.; Christians, J. A.; Morozov, Y. v; Mucunzi, A.; Manser, J. S.; Kamat, P. v; Luther, J. M.; Kuno, M. A Quantitative and Spatially Resolved Analysis of the

Performance-Bottleneck in High Efficiency, Planar Hybrid Perovskite Solar Cells †. / *Energy Environ. Sci* **2018**, *11*, 960.
(17) Mastroianni, S.; Heinz, F. D.; Im, J.-H.; Veurman, W.; Padilla, M.; Schubert, M. C.; Würfel, U.; Grätzel, M.; Park, N.-G.; Hinsch, A. Analysing the Effect of Crystal Size and Structure in Highly Efficient $CH_3NH_3PbI_3$ Perovskite Solar Cells by Spatially Resolved Photo- and Electroluminescence Imaging. *Nanoscale* **2015**, *7* (46), 19653–19662.
(18) Okano, M.; Endo, M.; Wakamiya, A.; Yoshita, M.; Akiyama, H.; Kanemitsu, Y. Degradation Mechanism of Perovskite $CH_3NH_3PbI_3$ Diode Devices Studied by Electroluminescence and Photoluminescence Imaging Spectroscopy. *Applied Physics Express* **2015**, *8* (10), 102302.
(19) Soufiani, A. M.; Tayebjee, M. J. Y.; Meyer, S.; Ho-Baillie, A.; Sung Yun, J.; MacQueen, R. W.; Spiccia, L.; Green, M. A.; Hameiri, Z. Electro- and Photoluminescence Imaging as Fast Screening Technique of the Layer Uniformity and Device Degradation in Planar Perovskite Solar Cells. *Journal of Applied Physics* **2016**, *120* (3), 035702.
(20) Schubert, M. C.; Mundt, L. E.; Walter, D.; Fell, A.; Glunz, S. W. Spatially Resolved Performance Analysis for Perovskite Solar Cells. *Advanced Energy Materials* **2020**, *10* (26), 1904001.
(21) Bui, A. D.; Mozaffari, N.; Truong, T. N.; Duong, T.; Weber, K. J.; White, T. P.; Catchpole, K. R.; Macdonald, D.; Nguyen, H. T. Electrical Properties of Perovskite Solar Cells by Illumination Intensity and Temperature-dependent Photoluminescence Imaging. *Progress in Photovoltaics: Research and Applications* **2021**, https://doi.org/10.1002/pip.3498.
(22) Rau, U.; Kirchartz, T. The Principle of Detailed Balance and the Opto-Electronic Properties of Solar Cells. In *Photon Management in Solar Cells*; John Wiley & Sons, Ltd, 2015; pp 21–48.
(23) Wong, J.; Green, M. A. From Junction to Terminal: Extended Reciprocity Relations in Solar Cell Operation. *Physical Review B - Condensed Matter and Materials Physics* **2012**, *85* (23), 235205.
(24) Rau, U.; Huhn, V.; Stoicescu, L.; Schneemann, M.; Augarten, Y.; Gerber, A.; Pieters, B. E. Photocurrent Collection Efficiency Mapping of a Silicon Solar Cell by a Differential Luminescence Imaging Technique. *Applied Physics Letters* **2014**, *105* (16), 163507.
(25) El-Hajje, G.; Momblona, C.; Gil-Escrig, L.; Ávila, J.; Guillemot, T.; Guillemoles, J. F.; Sessolo, M.; Bolink, H. J.; Lombez, L. Quantification of Spatial Inhomogeneity in Perovskite Solar Cells by Hyperspectral Luminescence Imaging. *Energy & Environmental Science* **2016**, *9* (7), 2286–2294.
(26) Ren, A.; Lai, H.; Hao, X.; Tang, Z.; Xu, H.; Yu Jeco, B. M. F.; Watanabe, K.; Wu, L.; Zhang, J.; Sugiyama, M.; Wu, J.; Zhao, D. Efficient Perovskite Solar Modules with Minimized Nonradiative Recombination and Local Carrier Transport Losses. *Joule* **2020**, *4* (6), 1263–1277.
(27) Stolterfoht, M.; le Corre, V. M.; Feuerstein, M.; Caprioglio, P.; Koster, L. J. A.; Neher, D. Voltage-Dependent Photoluminescence and How It Correlates with the Fill Factor and Open-Circuit Voltage in Perovskite Solar Cells. *ACS Energy Letters* **2019**, *4* (12), 2887–2892.
(28) Thiesbrummel, J.; le Corre, V. M.; Peña-Camargo, F.; Perdigón-Toro, L.; Lang, F.; Yang, F.; Grischek, M.; Gutierrez-Partida, E.; Warby, J.; Farrar, M. D.; Mahesh, S.; Caprioglio, P.; Albrecht, S.; Neher, D.; Snaith, H. J.; Stolterfoht, M. Universal Current Losses in

Perovskite Solar Cells Due to Mobile Ions. *Advanced Energy Materials* **2021**, *11* (34), 2101447.
(29) Du, T.; Xu, W.; Xu, S.; Ratnasingham, S. R.; Lin, C. T.; Kim, J.; Briscoe, J.; McLachlan, M. A.; Durrant, J. R. Light-Intensity and Thickness Dependent Efficiency of Planar Perovskite Solar Cells: Charge Recombination versus Extraction. *Journal of Materials Chemistry C* **2020**, *8* (36), 12648–12655.
(30) Caprioglio, P.; Stolterfoht, M.; Wolff, C. M.; Unold, T.; Rech, B.; Albrecht, S.; Neher, D. On the Relation between the Open-Circuit Voltage and Quasi-Fermi Level Splitting in Efficient Perovskite Solar Cells. *Advanced Energy Materials* **2019**, *9* (33), 1901631.
(31) Caprioglio, P.; Wolff, C. M.; Sandberg, O. J.; Armin, A.; Rech, B.; Albrecht, S.; Neher, D.; Stolterfoht, M. On the Origin of the Ideality Factor in Perovskite Solar Cells. *Advanced Energy Materials* **2020**, *10* (27), 2000502.
(32) Sarritzu, V.; Sestu, N.; Marongiu, D.; Chang, X.; Masi, S.; Rizzo, A.; Colella, S.; Quochi, F.; Saba, M.; Mura, A.; Bongiovanni, G. Optical Determination of Shockley-Read-Hall and Interface Recombination Currents in Hybrid Perovskites. *Scientific Reports* **2017**, *7* (1), 44629.
(33) Hameiri, Z.; Chaturvedi, P.; McIntosh, K. R. Imaging the Local Ideality Factor by Contactless Photoluminescence Measurement. *Applied Physics Letters* **2013**, *103* (2), 023501.
(34) Onno, A.; Chen, C.; Koswatta, P. Passivation, Conductivity, and Selectivity in Solar Cell Contacts: Concepts and Simulations Based on a Unified Partial-Resistances Framework. *J. Appl. Phys* **2019**, *126*, 183103.
(35) Tvingstedt, K.; Malinkiewicz, O.; Baumann, A.; Deibel, C.; Snaith, H. J.; Dyakonov, V.; Bolink, H. J. Radiative Efficiency of Lead Iodide Based Perovskite Solar Cells. *Scientific Reports 2014 4:1* **2014**, *4* (1), 1–7.
(36) Wurfel, P. The Chemical Potential of Radiation. *J. Phys. C: Solid State Phys* **1982**, *15*, 3967–3985.
(37) Hall, R. N. Electron-Hole Recombination in Germanium. *Physical Review* **1952**, *87* (2), 387.
(38) Shockley, W.; Read, W. T. Statistics of the Recombinations of Holes and Electrons. *Physical Review* **1952**, *87* (5), 835.
(39) Courtier, N. E. Interpreting Ideality Factors for Planar Perovskite Solar Cells: Ectypal Diode Theory for Steady-State Operation. *Physical Review Applied* **2020**, *14* (2), 024031.
(40) ANDOR (Oxford instruments). *Zyla SCMOS: Manufacturer Specification Sheet*.
(41) Kerr, M. J.; Cuevas, A.; Sinton, R. A. Generalized Analysis of Quasi-Steady-State and Transient Decay Open Circuit Voltage Measurements. *Journal of Applied Physics* **2001**, *91* (1), 399.
(42) Hinken, D.; Bothe, K.; Ramspeck, K.; Herlufsen, S.; Brendel, R. Determination of the Effective Diffusion Length of Silicon Solar Cells from Photoluminescence. *Journal of Applied Physics* **2009**, *105* (10), 104516.
(43) Rau, U.; Huhn, V.; Pieters, B. E. Luminescence Analysis of Charge-Carrier Separation and Internal Series-Resistance Losses in Cu (In,Ga)Se2 Solar Cells. *Physical Review Applied* **2020**, *14* (1), 014046.
(44) McCarthy, M. M.; Walter, A.; Moon, S. J.; Noel, N. K.; O'Brien, S.; Pemble, M. E.; Nicolay, S.; Wenger, B.; Snaith, H. J.; Povey, I. M. Atomic Layer Deposited Electron

Transport Layers in Efficient Organometallic Halide Perovskite Devices. *MRS Advances* **2018**, *3* (51), 3075–3084.
(45) Zhu, Z.; Bai, Y.; Liu, X.; Chueh, C. C.; Yang, S.; Jen, A. K. Y. Enhanced Efficiency and Stability of Inverted Perovskite Solar Cells Using Highly Crystalline SnO2 Nanocrystals as the Robust Electron-Transporting Layer. *Adv Mater* **2016**, *28* (30), 6478–6484.
(46) Liu, X.; Liu, Z.; Ye, H.; Tu, Y.; Sun, B.; Tan, X.; Shi, T.; Tang, Z.; Liao, G. Novel Efficient C60-Based Inverted Perovskite Solar Cells with Negligible Hysteresis. *Electrochimica Acta* **2018**, *288*, 115–125.
(47) Crameri, F. Scientific Colour Maps. *Zenodo* **2021**, https://zenodo.org/record/5501399.
(48) "Google LLC." Noto Emoji fonts https://github.com/googlefonts/noto-emoji (accessed 2021 -11 -22).